

Global Parametric Gates for Multi-qubit Entanglement

J.Z. Yang,¹ L.Guo,¹ H.N.Xiong,² J.H.Wang,³ Y.Li,¹ Y.F.Yang,¹
C.J.An,¹ H.Y.Zhang,^{1,4} L.Y.Sun,^{1,4} Y.P. Song,^{1,4,*} and L.M.Duan^{1,4,†}

¹Center for Quantum Information, Institute for Interdisciplinary Information Sciences, Tsinghua University, Beijing 100084, China

²Beijing Key Laboratory of Fault-Tolerant Quantum Computing, Beijing Academy of Quantum Information Sciences, Beijing 100193, China

³S Lab at Shenzhen's Quantum Science Center in the Guangdong Hongkong-Macao Greater Bay Area, 518045, China

⁴Hefei National Laboratory, Hefei 230088, China

We propose and experimentally demonstrate a global parametric gate that generates multi-qubit entangled states in a single step. By applying a parametric drive to a common qubit at precise detunings relative to computational qubits, we directly produce two-, three-, and four-qubit entanglement with state fidelities of $99.4\% \pm 0.2\%$, $93.4\% \pm 0.3\%$, and $91.4\% \pm 0.3\%$, respectively. This scheme enables efficient, reconfigurable control using only microwave drives and is compatible with fixed-frequency qubits. Error analyses indicate that infidelity stems primarily from decoherence and coherent control errors, with negligible contributions from static ZZ coupling and flux noise. Furthermore, simulations with state-of-the-art parameters predict this global gate can generate high-fidelity (99.70%) entanglement in systems of up to six qubits.

All quantum information technologies rely on a fundamental prerequisite: high-fidelity quantum operations. This includes high-fidelity gates[1–4], on-demand generation of entangled states [5–8], and precise coherent control [9–13]. Simulating quantum many-body systems is a key application for emerging quantum processors[14–17]. As superconducting processors scale toward increasingly complex qubit networks, two critical challenges emerge: developing fault-tolerant architectures resilient to component failures[18, 19], and significantly reducing the resource overhead for qubit control [20–22].

State-of-the-art superconducting quantum architectures currently employ either one-dimensional[9, 16, 23] or heavy-square lattice configurations[10, 18, 24, 25], where each transmon qubit incorporates independent XY and Z control lines for gate operations and frequency tuning. While these platforms have successfully demonstrated quantum advantage and enabled surface code error correction implementations, they remain vulnerable to network fragmentation from individual qubit failures. In addition, long-range interactions in many-body systems can give rise to rich physical phenomena and complex phase diagrams[26, 27]. However, conventional superconducting quantum architectures typically restrict interaction distances. A ring-network superconducting architecture features shared bus resonators - each ring contains a common bus resonator enabling all-to-all connectivity among qubits. By leveraging engineered long-range interactions and all-to-all connectivity, the ring structure inherently prevents network fragmentation from individual qubit failures, and thus enhances quantum processor robustness.

Quantum entanglement is a hallmark of quantum systems, distinguishing them from classical ones[7, 8]. However, preparing large-scale multi-qubit entangled states remains challenging, as it requires complete control over

the qubits and their noise environment. Multi-qubit entanglement has been demonstrated in platforms including superconducting circuits and ion traps[5–8, 28]. Conventional methods typically employ sequential two-qubit entangling gates, an approach whose scalability is constrained by qubit coherence. Exploiting global quantum gates that generate multi-qubit entanglement in a single-step would help reduce quantum circuit depth and improve simulation efficiency. Theoretical predictions suggest that global multi-qubit entangling gates with all-to-all connectivity could provide the key to achieving polynomial or even exponential speedups[29–31]. While parallel operations on five qubit pairs have been used to generate Greenberger-Horne-Zeilinger (GHZ) states[5], this method requires all qubits to be equally coupled to and detuned from a bus resonator, imposing fabrication challenges and necessitating flux tunability.

Furthermore, the gate scheme is expected to be compatible with fixed-frequency qubits with microwave-only control, reducing the resource overhead for qubit control. Such schemes have been investigated, including cross-resonance (CR) gate[32, 33], resonator-induced phase gate (RIP)[34], and proposed geometric phase gates[35, 36]. While the CR gate does not support a global gate scheme, the refocused RIP gate could realize a global entangling gate[34], but only if each qubit's frequency is individually tunable or by employing an echo trick. In this letter, we demonstrate a global entangling gate in a ring-network superconducting processor with a high-connectivity architecture, using a bus resonator for programmable inter-qubit coupling. By parametrically driving on a common qubit with precise frequency detunings relative to the computational qubits, we generate a four-qubit entangled state in a single step with a fidelity of 91.4% ($\pm 0.3\%$). This unique global gate scheme excels at producing multi-qubit entanglement efficiently,

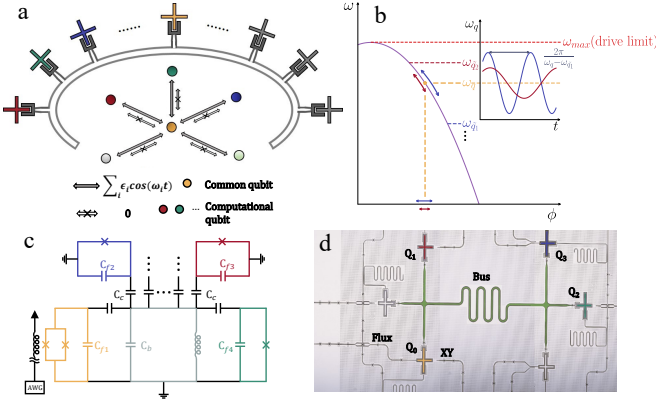


FIG. 1. Device architecture and gate principle. (a-b) Working principle of the global parametric gate. Multiple computational qubits (red, blue, green...) couple to a shared bus resonator, enabling all-to-all connectivity. Entanglement across multiple qubits is generated in a single step by applying a microwave parametric drive to a flux-tunable common qubit (yellow). The drive consists of a superposition of frequency components detuned from the fixed-frequency computational qubits. (c) Schematic circuit of the superconducting architecture featuring the shared bus resonator. The parametric drive is applied to the common qubit via its dedicated flux line. (d) False-colored optical image of the fabricated device.

offering reconfigurable control solely through parametric microwave drives. The method enables the use of fixed-frequency computational qubits, providing frequency selectivity while alleviating frequency crowding and minimizing sensitivity to environmental noise.

Working principle of global parametric gate. Figure 1(a),(b) illustrates the working principle of our global parametric gate. Here, the frequency-tunable common qubit is biased at an operational point, where the frequency deviation from the sweet spot is larger than its detuning from each computational qubit. We generate an effective coupling $g_{j,eff}$, between the common qubit and the j -th computational qubit mediated by the bus resonator, by applying a microwave drive to the common qubit's flux line. This drive is a superposition of the specific frequency components that detune the common qubit from each computational qubit, given by $\sum_j \Omega_j \sin(\Delta_j t + \phi_j)$, where $\Delta_j = \omega_j - \omega_0$ is the frequency detuning between the common qubit (ω_0) and the j -th computational qubit (ω_j). The coupling $g_{j,eff}$ can be tuned independently by modulating the amplitude Ω_j and phase ϕ_j of each drive frequency component. We initialize all qubits to the ground state $|0\rangle$. A π pulse is then applied to one qubit to prepare the initial state $|1\rangle|0\rangle^{\otimes j-1}$. Subsequently, the parametric drive is activated for a duration t , satisfying the condition $g_{j,eff}t = (n + \frac{1}{4})\pi$ for an integer n . This operation generates an j -qubit W state: $|W_j\rangle = \frac{1}{\sqrt{j}}(|100\cdots 0\rangle + |010\cdots 0\rangle + \cdots + |00\cdots 01\rangle)$, under the condition that

the coupling strength $g_{j,eff}$ is identical for all computational qubits to the common qubit. This gate scheme differs from conventional parametric approaches, which either use a microwave-driven tunable coupler for two-qubit gates[37–39] or generate multi-qubit states by sequentially applying two-qubit gates to qubit pairs[6].

Experimental setup. Our quantum processor consists of six transmon qubits (Q_0-Q_5) coupled to a shared bus resonator. For implementation of the global entangling gate, we use qubits Q_0 as the common qubit and Q_1-Q_3 as the computational qubits, as illustrated in Figure 1(d). All four qubits are negatively detuned from the bus resonator, with qubit frequencies $\omega_j/2\pi = 5.0408, 5.0992, 5.2056$, and 5.2347 GHz for $j=0,1,2,3$, respectively, and a resonator frequency $\omega_b/2\pi = 5.5208$ GHz. The measured coupling strengths between each qubit Q_j and the bus resonator— $h_j/2\pi = 17.3, 22.8, 18.2$, and 15.2 MHz—satisfy the dispersive condition $h_j \ll |\Delta_{j,b}|$, where $\Delta_{j,b} = \omega_j - \omega_b$.

The system Hamiltonian under the rotating-wave approximation (RWA) is given by (see Supplementary Material for details):

$$H = \sum_{j=0}^n \frac{\alpha_j}{2} a_j^\dagger a_j^\dagger a_j a_j + \sum_{j=1}^n g_j (a_0 a_j^\dagger e^{i\Delta_j t} + h.c.) + \sum_{j=1}^n \Omega_j \sin(\nu_j t + \phi_j) a_0^\dagger a_0 \quad (1)$$

Where $g_j = \frac{h_0 h_j}{2} \left(\frac{1}{\Delta_{0,b}} + \frac{1}{\Delta_{j,b}} \right)$, Ω_j and ν_j are the parametric drive amplitude and frequency for the qubit pair Q_0-Q_j . α_j denotes the anharmonicity of Q_j .

In the interaction picture, under the unitary transformation $U = \text{Exp}\{i \sum_{j=1}^n \epsilon_j \cos(\nu_j t + \phi_j) a_0^\dagger a_0\}$, the Hamiltonian becomes:

$$H_I = \sum_{j=1}^n g_j \left(a_0 a_j^\dagger e^{i\Delta_j t} e^{\sum_{j=1}^n \epsilon_j \cos(\nu_j t + \phi_j)} + h.c. \right) \quad (2)$$

where $\epsilon_j = \Omega_j/\nu_j$. When $\nu_j = \Delta_j$ and the effective drives, $\epsilon_1, \epsilon_2, \dots, \epsilon_j$, are identical, we obtain the final effective Hamiltonian,

$$H = \sum_{j=1}^n g_j J_1(\epsilon_j) \prod_{k \neq j} J_0(\epsilon_k) (i a_0 a_j^\dagger e^{i\phi_j} + h.c.) \quad (3)$$

This effective Hamiltonian describes a controllable exchange interaction with an effective coupling strength $g_{j,eff} = g_j J_1(\epsilon_j) \prod_{k \neq j} J_0(\epsilon_k)$, where J_n are Bessel functions of the first kind[37, 40].

We begin by characterizing the two-qubit parametric gate. The operating frequency of the common qubit, Q_0 , is set to 5.0408 GHz by applying a specific bias voltage to its flux line (see Supplementary Material). To account for the nonlinear frequency response, we modulate the parametric drive, causing the qubit frequency

oscillates symmetrically about its operational setpoint as $\Omega_j \sin(\nu_j t + \phi_j)$.

By applying the parametric modulation pulse on the common qubit, we measure the simultaneous quantum-state population of both qubits (e.g., Q_0 and Q_1) as a function of gate length and drive frequency. The resulting population exchange, shown in Figure 2(e), demonstrates coherent excitation oscillations between the qubits. The parametric flux modulation induces a DC shift in the common qubit's frequency[38, 39], which shifts the resonant exchange frequency from its un-driven value, $\nu_{j,\Omega_j=0}$, by approximately 8.3 MHz. In the upper panel of Figure 3(a), we plot the exchange oscillation between the two-qubit states $|01\rangle$ and $|10\rangle$ at the drive frequency that maximizes the inter-qubit quantum exchange. The oscillation period is determined by the effective coupling strength, $g_{j,eff}(\epsilon_j)$. In our experiments, we selected a drive amplitude that maximizes this strength, thereby minimizing the oscillation period, as detailed in the Supplementary Material. At specific locations in Figure 3(a), where $g_{j,eff}t = (n + \frac{1}{4})$, the excitation is equally shared between both qubits, and a maximally entangled state $\frac{\sqrt{2}}{2}(|01\rangle + i|10\rangle)$ can be generated[38, 39]. A pulse length satisfying $g_{j,eff}t = (n + \frac{1}{2})$ implements a primitive iSWAP gate, which can be used to construct a universal gate set for quantum computing. By applying a parametric drive with a uniform coupling strength $g_{j,eff}$ between the common qubit and all computational qubits, we observe exchange oscillations. These oscillations, starting from the initial states $|100\rangle$ and $|000\rangle$, are shown in the middle and lower panels of Figure 3(a). The entangled two-, three-, and four-qubit states are generated at gate times of 320 ns, 460 ns and 720 ns, respectively, which we verify using quantum state tomography.

Quantum State Tomography and Cross-entropy Benchmarking. We characterize the entangled state using quantum state tomography (QST), following the pulse sequence in Figure 3 (b) and (c). Using the Q_0 - Q_1 qubit pair as an example, we initialize both qubits to the ground state $|0\rangle$ and apply an X_π pulse to Q_1 . A parametric drive is then activated for 320 ns. Nine different single-qubit operations, $\{I, X_{\frac{\pi}{2}}, Y_{\frac{\pi}{2}}\} \otimes \{I, X_{\frac{\pi}{2}}, Y_{\frac{\pi}{2}}\}$, are applied to the two-qubit state right before a joint single-shot readout to perform state tomography. The resulting data, processed with maximum-likelihood estimation, yields the 16 Pauli traces used to reconstruct the two-qubit density matrix, ρ . The parametric drive induces a phase shift on both qubits. To compensate, we apply a virtual Z gate to each qubit to remove the measured phase offset. The achieved state fidelities, defined as $F(\rho, \sigma) = \sqrt{\sqrt{\rho}\sigma\sqrt{\rho}}$, are $99.4\% \pm 0.2\%$ for Q_0 - Q_1 and $99.0\% \pm 0.2\%$ for Q_0 - Q_2 , where σ is the density matrix of the ideal final state. Figure 2 (a) and (b) show a representative two-qubit state density matrix for Q_0 - Q_1 . Unless otherwise stated, all state and gate tomography results include post-selection on successful ground-state

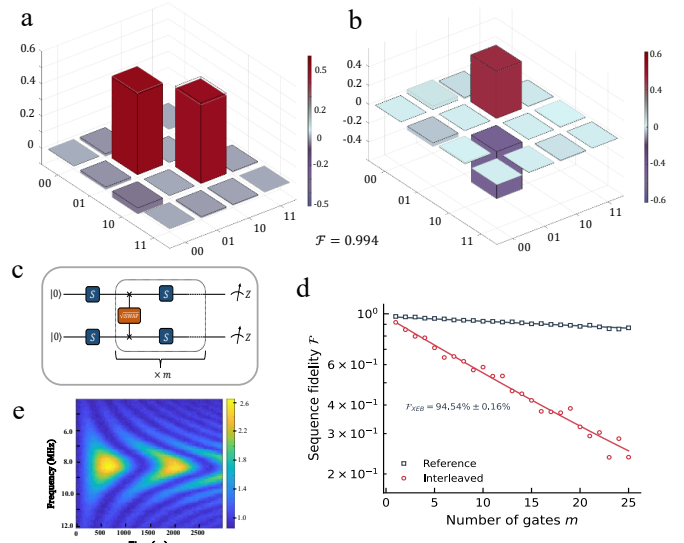


FIG. 2. Real part (a) and imaginary part (b) of a reconstructed 2-qubit density matrix for Q_0 - Q_1 ($F = 0.994(2)$, $t_{gate} = 320$ ns). Experimental results (colored bars) are compared to the ideal state (transparent bars). (c) Circuit schematic of the XEB sequence for the \sqrt{iSWAP} gate. The single-qubit gates S are randomly chosen from a set of 64 distinct single-qubit gates. (d) Fidelity decay for the \sqrt{iSWAP} gate ($t_{gate} = 316$ ns) and the reference gates as a function of the circuit depth m . (e) The exchange oscillation between $|10\rangle$ and $|01\rangle$ for Q_0 - Q_1 as a function of drive length and drive frequency ν_{1,Ω_1} relative to the qubit frequency detuning Δ_1 at $\Omega_1 = 0$. The parametric modulation induces a 8.3 MHz DC shift in Q_0 's frequency, offsetting the resonant exchange from $\nu_{1,\Omega_1=0}$.

initialization.

To characterize the two-qubit gate while eliminating state preparation and measurement (SPAM) errors, we perform cross-entropy benchmarking (XEB)[4, 10]. The protocol, illustrated in Figure 2(c), involves applying sequences of random single-qubit rotations chosen from a set of 64 distinct single-qubit gates. Each gate is a combination of a $\pi/2$ rotation around an axis in the xy-plane at $n\pi/8$ and a Z-rotation of $n\pi/8$ ($n = 0, 1, \dots, 7$). By measuring the output bitstrings x_i for each gate sequence, we calculate the standard XEB fidelity (F_{XEB}).

Precise calibration of the qubit and drive phases, as well as the common qubit's flux control line response, is crucial[41]. To this end, we employ a Cryoscope protocol to characterize the in situ flux, ϕ_{Q_0} , by measuring the step response of its dedicated flux control line at the chip level[42]. The Cryoscope measurement is a Ramsey-like protocol in which fixed-amplitude square flux pulses of varying durations are inserted between two $\pi/2$ pulses. The accumulated phase shift (ϕ) from the flux pulse reveals the qubit's on-chip frequency detuning, calculated as $\Delta\phi/\Delta t$. We convert this detuning into

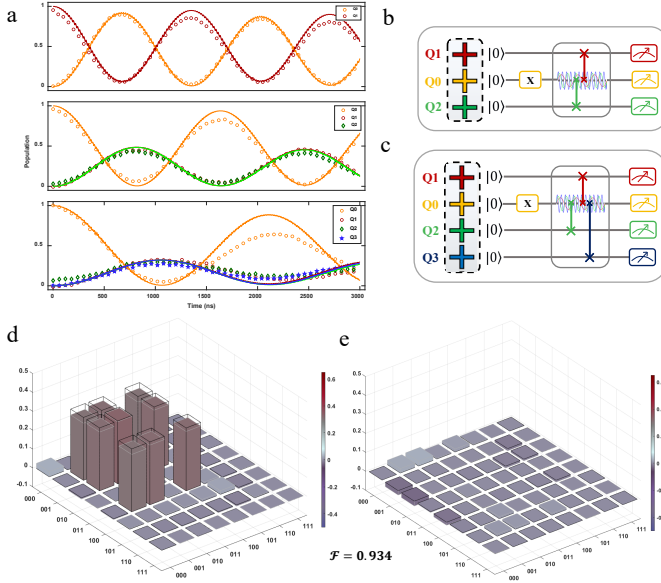


FIG. 3. (a) Qubit occupation probabilities during multi-qubit exchange oscillations. The upper, middle, and lower panels correspond to the two-qubit (Q_0-Q_1 , initial state $|01\rangle$), three-qubit ($Q_0-Q_1-Q_2$, initial state $|100\rangle$), and four-qubit ($Q_0-Q_1-Q_2-Q_3$, initial state $|1000\rangle$) systems, respectively. Experimental data are shown as colored markers, with simulation results as solid lines (Q_0 : yellow, cycle Q_1 : red, cycle Q_2 : green, diamond Q_3 : blue, pentagram). For the two-, three-, and four-qubit cases, the parametric drive frequencies are shifted by 8.3 MHz, 7.6 MHz, and 10.8 MHz, respectively, relative to the detuning between each computational qubit and the common qubit. Simulation parameters: $\Omega_1/2\pi=41.4$ MHz, $\nu_1/2\pi=58.4$ MHz (Q_0-Q_1); $\Omega_1/2\pi=29.9$ MHz, $\Omega_1:\Omega_2=1:3$, $\nu_1/2\pi=58.4$ MHz, $\nu_2/2\pi=164.8$ MHz ($Q_0-Q_1-Q_2$); $\Omega_1/2\pi=18.3$ MHz, $\Omega_1:\Omega_2:\Omega_3=1:3:4$, $\nu_1/2\pi=58.4$ MHz, $\nu_2/2\pi=164.8$ MHz, $\nu_3/2\pi=193.9$ MHz ($Q_0-Q_1-Q_2-Q_3$). (b, c) Pulse sequences used for quantum state tomography (QST) in three- and four-qubit entanglement experiments, respectively. (d, e) Real and imaginary parts of the reconstructed three-qubit density matrix for qubits $Q_0-Q_1-Q_2$ ($F = 0.934(3)$, $t_{gate}=460$ ns). Experimental results (colored bars) are compared to the ideal state (transparent bars).

a flux amplitude using the pre-calibrated qubit spectrum, yielding the response in a temporal resolution set by the time domain resolution of the flux pulse. To suppress flux ripples and correct phase errors, we then apply infinite impulse response (IIR) and finite impulse response (FIR) filters[42]. Following this calibration and optimization, we achieve an average \sqrt{i} SWAP gate fidelity of $94.54\%\pm0.16\%$ via cross-entropy benchmarking (XEB). Full methodological details are provided in the Supplementary Material.

We now benchmark the multi-qubit global gates using the quantum circuits depicted in Figure 3 (b) and (c), which are designed to generate entangled three- and four-qubit W states, followed by implementing QST on

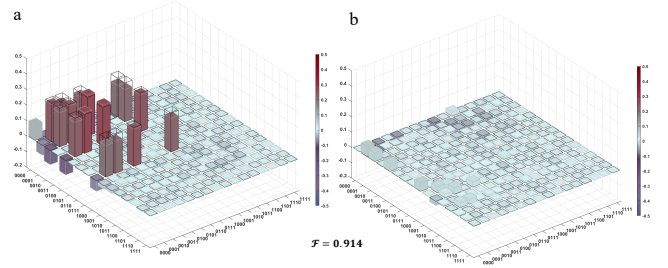


FIG. 4. Quantum state tomography of four-qubit entanglement. Real (a) and imaginary (b) parts of the reconstructed four-qubit density matrix for qubits $Q_0-Q_1-Q_2-Q_3$, measured after a gate time (t_{gate}) of 720 ns. The achieved state fidelity is $0.914(3)$. Experimental results are shown as colored bars, overlaid with the ideal state (transparent bars) for comparison.

the resulting quantum states. We first calibrate the optimal drive amplitude Ω_j for each parametric component to achieve identical oscillation periods across all qubit pairs. The operational frequency detuning and coupling strength vary among the computational qubits and the common qubit. As a result, the three- and four-qubit gate times differ from that of a specific two-qubit gate. Similar to the two-qubit operation, we initialize all qubits to the ground state $|0\rangle$, apply a π -pulse to Q_0 , and then activate the parametric drive for 460 ns (three-qubit case) and 720 ns (four-qubit case). Measurements in the $X(Y, Z)$ basis are achieved by inserting a Pauli $Y(X, I)$ rotation on each qubit before readout. This yields a total of 64 (8×8) and 256 (16×16) Pauli trace datasets for the three- and four-qubit states, respectively, with each dataset comprising $N = 10000$ repetitions. Finally, we reconstruct the density matrix ρ using maximum-likelihood estimation. We achieve state fidelities of $93.4\%\pm0.3\%$ and $91.4\%\pm0.3\%$ for the three- and four-qubit W states, respectively. The representative experimental density matrices and ideal matrices are presented in Figure 3(d)(e) and Figure 4(a)(b).

Error budget analysis. We conduct an error budget analysis to verify the sources of gate error, isolating the contributions from incoherent and coherent noise. A quantum error channel can be described by Kraus operators as $\varepsilon(\rho) = \sum_k K_k \rho K_k^\dagger$, $\sum_k K_k^\dagger K_k = I$ where ρ and I denote the state density and identity operator, respectively. The average fidelity for d -dimensional systems is given by $F = \frac{1}{d(d+1)} \sum_k [\text{Tr}(K_k^\dagger K_k) + |\text{Tr}(K_k)|^2]$ [2, 3, 43], where d is the dimension of the computational subspace. Based on the Kraus operators, the incoherent errors arose from the relaxation (T_1^q) and pure dephasing (T_ϕ^q) of the q th qubit, can be calculated as $\alpha \cdot t_g \sum_q \left(\frac{1}{T_1^q} + \frac{1}{T_\phi^q} \right)$, with a gate time t_g and a prefactor of $\alpha=2/5, 4/9$ and $8/17$ for the two-, three- and four-qubit system, respectively (see Supplementary Material for details)[2, 44]. Using

the qubit coherence time data (see Supplementary Material), we calculate coherence-limited infidelities of 1.44%, 3.35%, and 7.87% for the two-, three- and four-qubit gate (Q_0 - Q_1 , Q_0 - Q_1 - Q_2 , Q_0 - Q_1 - Q_2 - Q_3), respectively.

We next consider the flux-noise-induced error from the parametric drive on the common qubit (Q_0), which is sensitive to magnetic flux fluctuations through its Josephson junction loop. We analyze the T_2^{Echo} data for Q_0 using the formula $P_{|1\rangle} = A + Be^{-\Gamma t - (\Gamma_\phi^E t)^2}$, where Γ accounts for the effects of energy relaxation (T1) and white noise, while Γ_ϕ^E quantifies the dephasing from $1/f$ noise. The flux noise amplitude $\sqrt{A_\Phi}$ is extracted using $\Gamma_\phi^E = \sqrt{\ln 2} \left| \frac{\partial \omega}{\partial \Phi} \right| \sqrt{A_\Phi}$, where $S_\phi = A_\Phi/\omega$ and S_ϕ is the flux-noise spectral density ($\sqrt{A_\Phi} = 2.45 \mu\phi_0$) [1, 2, 45]. Numerical simulations show that the flux-noise-induced incoherent error for the implemented gate (320–720 ns) is on the order of 10^{-4} , which is negligible at the current stage.

Numerical simulations. To further investigate potential error sources, we perform numerical simulations using the generalized Hamiltonian of [Eq. \(S1\)](#), which includes higher-level states. These simulations incorporate qubit decoherence, dephasing, flux noise, and spurious ZZ interactions (see Supplementary Material for details). All simulation parameters are set to their experimentally measured values. The state fidelity is calculated with $F(\rho, \sigma) = \sqrt{\sqrt{\rho}\sigma\sqrt{\rho}}$, where σ is the density matrix of the ideal final state and ρ is the simulated density matrix. We estimated the gate fidelity by either simulating the evolution of the gate unitary operator or averaging the state fidelities over 36 initial two-qubit states. These states form the set $\{|0\rangle, |1\rangle, \frac{\sqrt{2}}{2}(|0\rangle \pm |1\rangle), \frac{\sqrt{2}}{2}(|0\rangle \pm i|1\rangle)\}^{\otimes 2}$, which are generated from the six standard initial single-qubit states.

We first simulate the exchange oscillations for the two-, three-, and four-qubit states; the results are plotted as solid lines in [Figure 3\(a\)](#). The simulated oscillations show good agreement with the experimental data without the use of any tunable parameters. Two-qubit quantum state tomography (QST) simulations yield entangled state fidelities of 99.39% for the Q_0 - Q_1 pair and 99.38% for the Q_0 - Q_2 pair, using the initial states in $\{|0\rangle, |1\rangle\}^{\otimes 2}$. These results agree with the experimentally measured fidelities. Decoherence and dephasing account for an infidelity of 0.60% for Q_0 - Q_1 and 0.61% for Q_0 - Q_2 . A negligible infidelity of less than 10^{-4} is attributed to unwanted static ZZ interaction. Furthermore, when comparing the 36 initial states, we find that the fidelities for states in $\{|0\rangle, |1\rangle\}^{\otimes 2}$ (99.39%) are higher than those in $\{|+\rangle, |i+\rangle\}^{\otimes 2}$ (96.57%). This indicates that the latter states are more susceptible to decoherence/dephasing error.

The simulated gate fidelity for pair Q_0 - Q_1 (Q_0 - Q_2) is 98.22% (97.84%), with infidelities of 1.53% (1.72%) from decoherence/dephasing and 0.08% (0.23%) from the

static ZZ interaction. This is higher than the experimental XEB fidelity of $94.54\% \pm 0.16\%$ (Q_0 - Q_1), revealing a discrepancy of 3.68% that we attribute to other coherent control imperfections.

Finally, quantum state tomography simulations for the three- and four-qubit entangling states achieve fidelities of 98.99% and 98.34%, respectively. The primary simulated infidelities are 0.99% and 1.64%, attributed to decoherence and dephasing, while the static ZZ interaction and flux noise are negligible contributors, both on the order of 10^{-4} . However, the experimentally measured fidelities are lower, at 93.4% and 91.4%. The discrepancies of approximately 5.59% and 6.94% are primarily due to SPAM errors and other coherent control errors, which are not included in the simulation.

Based on the above analyses, we conclude that the error in the multiparticle entanglement state generated by the global parametric scheme originates primarily from decoherence and coherent control errors. In contrast, the contributions from static ZZ and flux noise are negligible, on the order of 10^{-4} . These error sources and their corresponding budgets are summarized in [Table I](#).

Discussion and summary. The W state is a valuable resource in quantum information processing due to its robustness and persistent entanglement [46], making it suitable for tasks where quantum networks and communication are involved, and where the loss of qubits is a concern. Reducing the frequency detuning between the common and computational qubits while enhancing their interaction with the bus significantly shortens gate time, thereby suppressing decoherence error. For example, simulation shows that a \sqrt{iSWAP} gate can be realized in 50 ns with a frequency detuning of 100 MHz ($\Delta_1/2\pi = 100.0$ MHz, $\omega_b/2\pi = 5.1922$ GHz) and a qubit-bus coupling of 30 MHz ($h_{0,1}/2\pi = 30$ MHz), with all other parameters matching those in [Figure 3\(a\)](#). Using state-of-the-art superconducting qubit parameters (see Supplementary Material), we simulate the generation of entangled states via parametric global gates in two- to six-qubit systems, accounting for decoherence, static ZZ coupling, and flux noise. The resulting state fidelities are 99.91%, 99.88%, 99.85%, 99.80%, and 99.70%, respectively, well above the threshold for genuine multipartite entanglement of W states [47]. This implies that within a hexagonal ring-network lattice, high-fidelity intra-ring multipartite entanglement can be generated in a single step. Furthermore, by parametrically driving the common qubit shared between adjacent rings, we can also achieve multi-qubit entanglement across the lattice. This scheme thus enables long-range interactions and creation of multipartite entangled states across a honeycomb superconducting lattice.

TABLE I. Simulated error sources for the two-, three-, and four-qubit entanglement. Simulation parameters: 1: $\Omega_1/2\pi=44.6$ MHz, $\nu_1/2\pi=58.4$ MHz, $t_{gate}=320$ ns (Q_0 - Q_1); 2: $\Omega_2/2\pi=136.1$ MHz, $\nu_2/2\pi=154.9$ MHz, $t_{gate}=365$ ns (Q_0 - Q_1); 3: $\Omega_1/2\pi=32.6$ MHz, $\Omega_1:\Omega_2=1:3$, $\nu_1/2\pi=58.4$ MHz, $\nu_2/2\pi=164.8$ MHz, $t_{gate}=460$ ns (Q_0 - Q_1 - Q_2); 4: $\Omega_1/2\pi=18.3$ MHz, $\Omega_1:\Omega_2:\Omega_3=1:3:4$, $\nu_1/2\pi=58.4$ MHz, $\nu_2/2\pi=164.8$ MHz, $\nu_3/2\pi=193.9$ MHz, $t_{gate}=720$ ns (Q_0 - Q_1 - Q_2 - Q_3); 5: $\Omega_1/2\pi=55$ MHz, $\nu_1/2\pi=59.4$ MHz, $t_{gate}=316$ ns (Q_0 - Q_1); 6: $\Omega_2/2\pi=135$ MHz, $\nu_2/2\pi=154.0$ MHz, $t_{gate}=366$ ns (Q_0 - Q_2). Columns show the breakdown of simulated infidelity contributions: ϵ_{decoh} (decoherence/dephasing), ϵ_{ZZ} (static ZZ interaction), and ϵ_{flux} (flux noise).

Device	\mathcal{F}_{sim}	ϵ_{decoh}	ϵ_{ZZ}	ϵ_{flux}	\mathcal{F}_{exp}
2Q QST (Q_0 - Q_1)	99.39%	0.60%	1.1×10^{-5}	1.9×10^{-5}	$99.4\% \pm 0.2\%$
2Q QST (Q_0 - Q_2)	99.38%	0.61%	1.2×10^{-5}	2.7×10^{-5}	$99.0\% \pm 0.2\%$
3Q QST (Q_0 - Q_1 - Q_2)	98.99%	0.99%	3.3×10^{-4}	3.1×10^{-4}	$93.4\% \pm 0.3\%$
4Q QST (All)	98.34%	1.64%	6.4×10^{-4}	7.2×10^{-4}	$91.4\% \pm 0.3\%$
Gate (Q_0 - Q_1)	98.22%	1.53%	8.0×10^{-4}	1.2×10^{-3}	$94.54\% \pm 0.16\%$
Gate (Q_0 - Q_2)	97.84%	1.72%	2.3×10^{-3}	1.5×10^{-3}	—

ACKNOWLEDGEMENTS

We thank Haiyan Wang and Yue Jiang for the technical support. This work is supported by Quantum Science and Technology-National Science and Technology Major Project, Grant No. 2021ZD0301700.

AUTHOR CONTRIBUTIONS

L.M.D. and Y.P.S supervised the project. Y.P.S and J.Z.Y performed the measurements and simulations. Y.P.S fabricated the device. Y.P.S wrote the manuscript with feedback from all authors, and J.Z.Y. wrote specific sections of the supplementary materials.

COMPETING INTERESTS

The authors declare no competing interests.

* ypsong@mail.tsinghua.edu.cn
† lumingduan@tsinghua.edu.cn

[1] Y. Sung, L. Ding, J. Braumüller, A. Vepsäläinen, B. Kannan, M. Kjaergaard, A. Greene, G. O. Samach, C. McNally, D. Kim, *et al.*, Physical Review X **11**, 021058 (2021).

[2] R. Li, K. Kubo, Y. Ho, Z. Yan, Y. Nakamura, and H. Goto, Physical Review X **14**, 041050 (2024).

[3] L. Ding, M. Hays, Y. Sung, B. Kannan, J. An, A. Di Paolo, A. H. Karamlou, T. M. Hazard, K. Azar, D. K. Kim, *et al.*, Physical Review X **13**, 031035 (2023).

[4] Y. Kim, A. Morvan, L. B. Nguyen, R. K. Naik, C. Jünger, L. Chen, J. M. Kreikebaum, D. I. Santiago, and I. Siddiqi, Nature physics **18**, 783 (2022).

[5] C. Song, K. Xu, W. Liu, C.-p. Yang, S.-B. Zheng, H. Deng, Q. Xie, K. Huang, Q. Guo, L. Zhang, *et al.*, Physical Review Letters **119**, 180511 (2017).

[6] M. Reagor, C. B. Osborn, N. Tezak, A. Staley, G. Prawiroatmodjo, M. Scheer, N. Alidoust, E. A. Sete, N. Didier, M. P. da Silva, *et al.*, Science Advances **4**, eaao3603 (2018).

[7] M. Gong, M.-C. Chen, Y. Zheng, S. Wang, C. Zha, H. Deng, Z. Yan, H. Rong, Y. Wu, S. Li, *et al.*, Physical Review Letters **122**, 110501 (2019).

[8] N. Friis, O. Marty, C. Maier, C. Hempel, M. Holzapfel, P. Jurcevic, M. B. Plenio, M. Huber, C. Roos, R. Blatt, *et al.*, Physical Review X **8**, 021012 (2018).

[9] R. Barends, J. Kelly, A. Megrant, A. Veitia, D. Sank, E. Jeffrey, T. C. White, J. Mutus, A. G. Fowler, B. Campbell, *et al.*, Nature **508**, 500 (2014).

[10] F. Arute, K. Arya, R. Babbush, D. Bacon, J. C. Bardin, R. Barends, R. Biswas, S. Boixo, F. G. Brandao, D. A. Buell, *et al.*, Nature **574**, 505 (2019).

[11] S. Boixo, S. V. Isakov, V. N. Smelyanskiy, R. Babbush, N. Ding, Z. Jiang, M. J. Bremner, J. M. Martinis, and H. Neven, Nature Physics **14**, 595 (2018).

[12] K. A. Landsman, C. Figgatt, T. Schuster, N. M. Linke, B. Yoshida, N. Y. Yao, and C. Monroe, Nature **567**, 61 (2019).

[13] J.-H. Wang, T.-Q. Cai, X.-Y. Han, Y.-W. Ma, Z.-L. Wang, Z.-H. Bao, Y. Li, H.-Y. Wang, H.-Y. Zhang, L.-Y. Sun, *et al.*, Physical Review Research **4**, 043141 (2022).

[14] B. Fauseweh, Nature Communications **15**, 2123 (2024).

[15] P. J. O’Malley, R. Babbush, I. D. Kivlichan, J. Romero, J. R. McClean, R. Barends, J. Kelly, P. Roushan, A. Tranter, N. Ding, *et al.*, Physical Review X **6**, 031007 (2016).

[16] P. Roushan, C. Neill, J. Tangpanitanon, V. M. Bastidas, A. Megrant, R. Barends, Y. Chen, Z. Chen, B. Chiaro, A. Dunsworth, *et al.*, Science **358**, 1175 (2017).

[17] N. Maskara, S. Ostermann, J. Shee, M. Kalinowski, A. McClain Gomez, R. Araiza Bravo, D. S. Wang, A. I. Krylov, N. Y. Yao, M. Head-Gordon, *et al.*, Nature Physics **21**, 289 (2025).

[18] R. Versluis, S. Poletto, N. Khammassi, B. Tarasinski, N. Haider, D. J. Michalak, A. Bruno, K. Bertels, and L. DiCarlo, Physical Review Applied **8**, 034021 (2017).

[19] C. Chamberland, G. Zhu, T. J. Yoder, J. B. Hertzberg, and A. W. Cross, *Physical Review X* **10**, 011022 (2020).

[20] G. Li, Y. Ding, and Y. Xie, in *Proceedings of the twenty-fifth international conference on architectural support for programming languages and operating systems* (2020) pp. 1031–1045.

[21] J. M. Gambetta, J. M. Chow, and M. Steffen, *npj quantum information* **3**, 2 (2017).

[22] A. W. Cross, L. S. Bishop, S. Sheldon, P. D. Nation, and J. M. Gambetta, *Physical Review A* **100**, 032328 (2019).

[23] J. Kelly, R. Barends, A. G. Fowler, A. Megrant, E. Jeffrey, T. C. White, D. Sank, J. Y. Mutus, B. Campbell, Y. Chen, *et al.*, *Nature* **519**, 66 (2015).

[24] M. Takita, A. W. Cross, A. D. Córcoles, J. M. Chow, and J. M. Gambetta, *Physical Review Letters* **119**, 180501 (2017).

[25] M. Gong, S. Wang, C. Zha, M.-C. Chen, H.-L. Huang, Y. Wu, Q. Zhu, Y. Zhao, S. Li, S. Guo, *et al.*, *Science* **372**, 948 (2021).

[26] N. Defenu, T. Donner, T. Macrì, G. Pagano, S. Ruffo, and A. Trombettoni, *Reviews of Modern Physics* **95**, 035002 (2023).

[27] C. Lyu, X. Tang, J. Li, X. Xu, M.-H. Yung, and A. Bayat, *New Journal of Physics* **25**, 053022 (2023).

[28] Y. Wang, Y. Li, Z.-q. Yin, and B. Zeng, *npj Quantum information* **4**, 46 (2018).

[29] Y. Lu, S. Zhang, K. Zhang, W. Chen, Y. Shen, J. Zhang, J.-N. Zhang, and K. Kim, *Nature* **572**, 363 (2019).

[30] D. Maslov and Y. Nam, *New Journal of Physics* **20**, 033018 (2018).

[31] E. A. Martinez, T. Monz, D. Nigg, P. Schindler, and R. Blatt, *New Journal of Physics* **18**, 063029 (2016).

[32] S. Sheldon, E. Magesan, J. M. Chow, and J. M. Gambetta, *Physical Review A* **93**, 060302 (2016).

[33] T.-Q. Cai, X.-Y. Han, Y.-K. Wu, Y.-L. Ma, J.-H. Wang, Z.-L. Wang, H.-Y. Zhang, H.-Y. Wang, Y.-P. Song, and L.-M. Duan, *Physical Review Letters* **127**, 060505 (2021).

[34] H. Paik, A. Mezzacapo, M. Sandberg, D. T. McClure, B. Abdo, A. D. Córcoles, O. Dial, D. F. Borgorin, B. Plourde, M. Steffen, *et al.*, *arXiv preprint arXiv:1606.00685* (2016).

[35] T.-Q. Cai, J.-H. Wang, Z.-L. Wang, X.-Y. Han, Y.-K. Wu, Y.-P. Song, and L.-M. Duan, *Physical Review Research* **3**, 043071 (2021).

[36] S.-L. Zhu and Z. Wang, *Physical Review Letters* **91**, 187902 (2003).

[37] X. Li, Y. Ma, J. Han, T. Chen, Y. Xu, W. Cai, H. Wang, Y.-P. Song, Z.-Y. Xue, Z.-q. Yin, *et al.*, *Physical Review Applied* **10**, 054009 (2018).

[38] D. C. McKay, S. Filipp, A. Mezzacapo, E. Magesan, J. M. Chow, and J. M. Gambetta, *Physical Review Applied* **6**, 064007 (2016).

[39] X. Han, T. Cai, X. Li, Y. Wu, Y. Ma, Y. Ma, J. Wang, H. Zhang, Y. Song, and L. Duan, *Physical Review A* **102**, 022619 (2020).

[40] Y. Wu, L.-P. Yang, M. Gong, Y. Zheng, H. Deng, Z. Yan, Y. Zhao, K. Huang, J. Clark, W. J. Munro, *et al.*, *npj Quantum Information* **4**, 50 (2018).

[41] B. R. Johnson, *Controlling photons in superconducting electrical circuits* (Yale University, 2011).

[42] M. A. Rol, L. Ciorciaro, F. K. Malinowski, B. M. Tarasinski, R. E. Sagastizabal, C. C. Bultink, Y. Salathe, N. Haandbæk, J. Sedivy, and L. DiCarlo, *Applied Physics Letters* **116** (2020).

[43] L. H. Pedersen, N. M. Møller, and K. Mølmer, *Physics Letters A* **367**, 47 (2007).

[44] M. A. Nielsen and I. L. Chuang, *Quantum computation and quantum information* (Cambridge university press, 2010).

[45] J. Braumüller, L. Ding, A. P. Vepsäläinen, Y. Sung, M. Kjaergaard, T. Menke, R. Winik, D. Kim, B. M. Niedzielski, A. Melville, *et al.*, *Physical Review Applied* **13**, 054079 (2020).

[46] G. Park, H. F. Hofmann, R. Okamoto, and S. Takeuchi, *Science Advances* **11**, eadx4180 (2025).

[47] P. Lougovski, S. J. van Enk, K. S. Choi, S. B. Papp, H. Deng, and H. Kimble, *New Journal of Physics* **11**, 063029 (2009).

[48] F. Motzoi, J. M. Gambetta, P. Rebentrost, and F. K. Wilhelm, *Physical Review Letters* **103**, 110501 (2009).

[49] A. Kamal, A. Marblestone, and M. Devoret, *Physical Review B—Condensed Matter and Materials Physics* **79**, 184301 (2009).

[50] K. W. Murch, S. Weber, C. Macklin, and I. Siddiqi, *Nature* **502**, 211 (2013).

[51] P. Mundada, G. Zhang, T. Hazard, and A. Houck, *Physical Review Applied* **12**, 054023 (2019).

[52] M. Kounalakis, C. Dickel, A. Bruno, N. Langford, and G. Steele, *npj Quantum Information* **4**, 38 (2018).

[53] H. Xiong, J. Wang, J. Song, J. Yang, Z. Bao, Y. Li, Z.-Y. Mi, H. Zhang, H.-F. Yu, Y. Song, *et al.*, *arXiv preprint arXiv:2502.18902* (2025).

[54] D. I. Schuster, *Circuit quantum electrodynamics* (Yale University, 2007).

[55] J. R. Johansson, P. D. Nation, and F. Nori, *Computer Physics Communications* **183**, 1760 (2012).

Supplementary Material

CONTENTS

Contents	1
Device fabrication	1
Measurement setup	1
Device parameters	1
Theory	4
Calibration of parametric drive amplitude and frequency	5
XEB	6
Cryoscope measurement	7
QST data for Q_0 - Q_2	8
Decoherence error	8
Numerical simulations	10

DEVICE FABRICATION

The device fabrication involves three primary steps: (1) A c-plane sapphire substrate is chemically cleaned with piranha solution, annealed, and then coated with a tantalum (Ta) film via sputtering deposition. Photolithography and inductively coupled-plasma (ICP) etching are subsequently used to define all base wiring and resonators. (2) Two photolithography processes, followed by Ta deposition and wet etching, are employed to construct air bridges. These structures primarily serve to connect segments of ground plane, thereby reducing parasitic slotline modes. (3) Josephson junctions are fabricated using electron-beam (e-beam) lithography with two layers of e-beam resists (A4/EL11) and a double-angle aluminum deposition process. Prior to spin-coating the e-beam resists, the chip undergoes sequential treatment in TAMI, piranha solution, and buffered oxide etch (BOE). We optimized the sputtering conditions—including pressure, deposition rate, substrate temperature, and target-to-substrate distance—to produce high-quality alpha-phase tantalum films.

MEASUREMENT SETUP

Our measurement circuit is depicted in [Figure S1](#). The quantum processor is mounted in an aluminium sample holder at a base temperature of 10mK in a dilution refrigerator, protected with a magnetic shielding and an infrared shielding. Full qubit control is implemented using four synchronized Arbitrary Waveform Generators (AWGs, Tek5014C), which supply six pairs of sideband-modulated signals for XY and readout control. These XY and readout control signals are generated from a single microwave source, modulated at different sideband frequencies. One analog channel of an AWG is dedicated to generating the parametric modulation pulse and Z control for the common qubit. This method of control guarantees stable phase differences during the quantum tomography experiments. To minimize phase errors and leakage to higher transmon levels, we employ Derivative Removal Adiabatic Gate (DRAG) pulses for pulse correction and single-qubit rotations [\[48\]](#).

For readout, six cavities are coupled to two separate transmission lines, each connected to a Josephson Parametric Amplifier (JPA) [\[49, 50\]](#). The JPA is pumped and biased by a signal generator and a DC voltage source (YOKOGAWA GS210), providing approximately 20 dB of gain with a bandwidth of about 300 MHz at 10 mK. It serves as the first amplification stage, followed by a high-electron mobility transistor amplifier at 4 K and additional amplifiers at room temperature. This configuration enables high-fidelity, simultaneous single-shot readout of all qubits. The JPA circuit design employs standard 50Ω impedance matching without further impedance engineering. The detailed measurement and readout techniques can be found in Ref.[\[13, 33, 39\]](#)

DEVICE PARAMETERS

Our quantum processor comprises six transmon qubits (Q_0 - Q_5) coupled to a shared bus resonator, as shown in [Figure 1\(d\)](#) in the main text. We use four qubits (Q_0 - Q_3) to implement the global entangling gate. Q_1 and Q_2 are

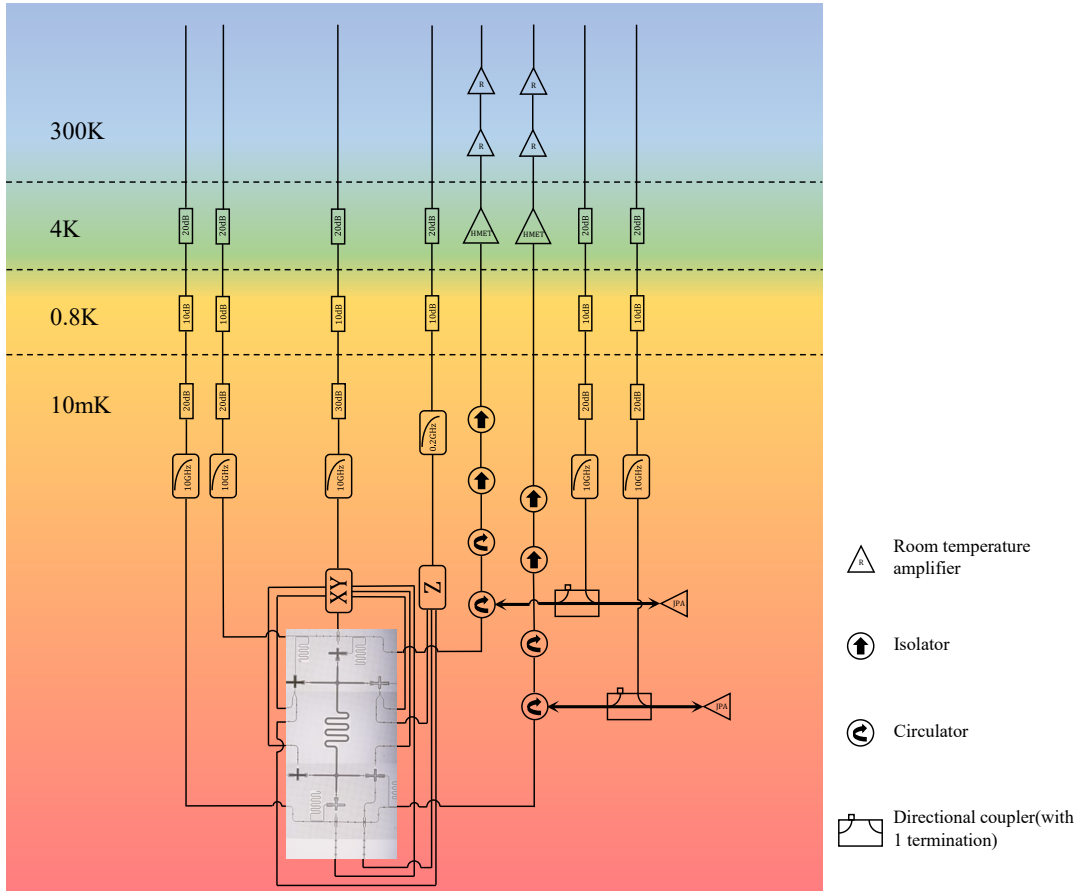


FIG. S1. **Experimental setup and cryogenic wiring diagram.** The schematic illustrates the signal path for qubit control and measurement. Control signals (XY, Z, parametric drive) generated at room temperature are progressively attenuated and filtered at different temperature stages of the dilution refrigerator before reaching the quantum processor at $\sim 10\text{ mK}$. Readout signals from the device are amplified by a near-quantum-limited Josephson Parametric Amplifier (JPA) at the base temperature, followed by a HEMT amplifier at 4 K and further amplification at room temperature before demodulation and acquisition.

fixed frequency qubits, while Q_0 and Q_3 have their individual flux line for frequency tuning. Each qubit is coupled to an independent Purcell-filtered cavity for individual readout. The readout signals for qubits Q_0 - Q_2 are multiplexed onto one transmission line, while those for qubits Q_3 - Q_5 are multiplexed onto a second, separate line.

We measure each qubit's energy relaxation time (T_1), Ramsey dephasing time (T_2), and echo dephasing time (T_2^{Echo}), as well as the inter-qubit couplings. The resulting device parameters are summarized in Table S2.

The coupling between higher energy levels of qubits gives rise to a cross-Kerr term $\xi_{ZZ}a_1^\dagger a_1 a_2^\dagger a_2$, resulting in a static ZZ interaction [39, 51, 52]. We define $\xi_{ZZ} = \hbar(\omega_{11} - \omega_{01} - \omega_{10})$ as the static ZZ coupling strength with respect to performance of single-qubit gates. We measure the static ZZ interaction by a Ramsey-type measurement, which involves probing the frequency shift of Q_1 with initializing Q_2 in either its ground or excited state.

We measure the coupling strength between each qubit and the bus by probing the qubit frequency shift induced by photon number splitting. A pump pulse is sent to the bus to displace the photon state followed by a probe pulse on the qubit to detect its frequency. We obtain qubit spectrum with coherent bus drive at different average cavity occupations (n). Figure S3 shows a representative qubit spectrum for Q_3 . To improve the spectral resolution, a long probe pulse of 5000 ns is used. The qubit response is observed at frequencies $\omega_q + 2n\chi$ ($n = 0, 1, 2, \dots$) corresponding to the bus being in the Fock state $|n\rangle$ [53, 54]. The coupling strength h_j is extracted by $\chi = -\frac{h_j^2\alpha}{\Delta_{j,b}(\Delta_{j,b} - \alpha)}$ [54], where α_j is the anharmonicity of the qubit, and $\Delta_{j,b} = \omega_q - \omega_b$.

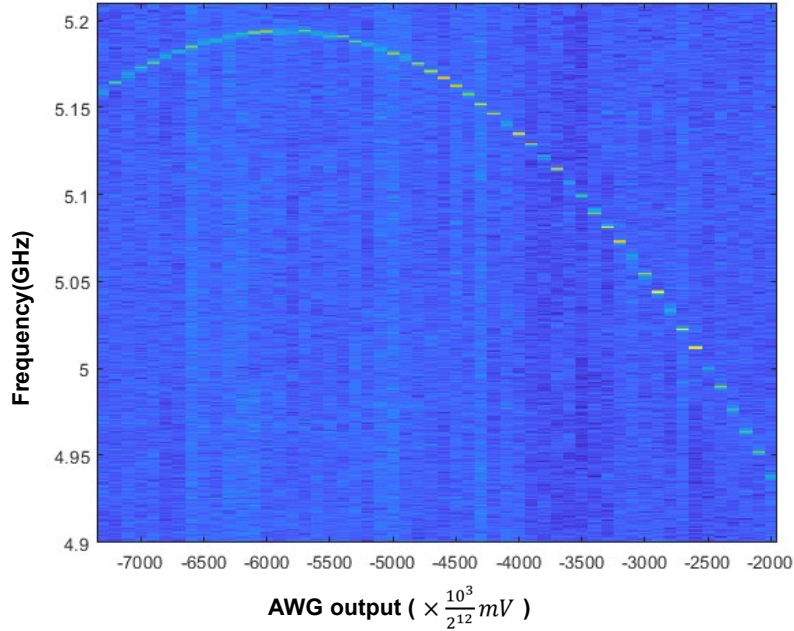


FIG. S2. **Flux map of the common qubit Q_0 .** The transition frequency of Q_0 is plotted as a function of the DC voltage bias applied to its dedicated flux line via an Arbitrary Waveform Generator (AWG). The characteristic parabolic dependence is visible, with the maximum frequency corresponding to the flux-insensitive "sweet spot". This map is used to precisely calibrate the DC bias and AC modulation amplitudes required for parametric gate operations.

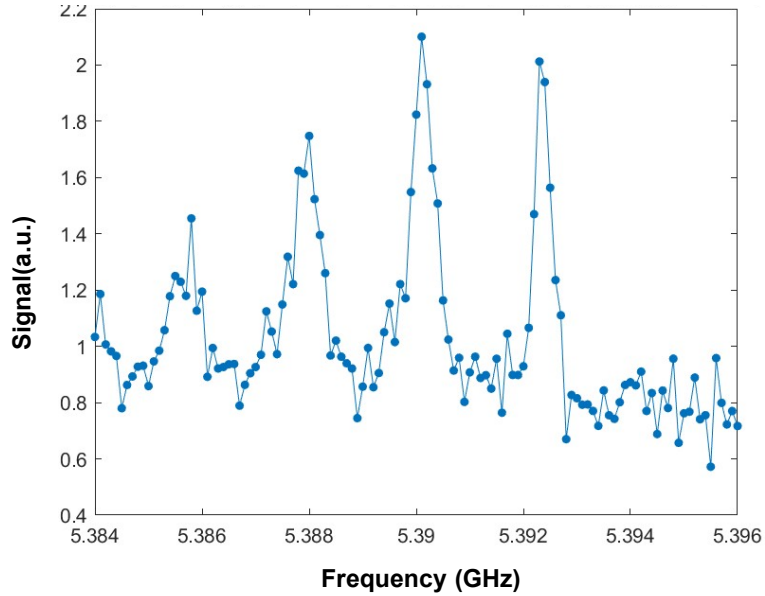


FIG. S3. **Resonator-induced photon number splitting of Q_0 .** The spectrum of qubit Q_3 is measured while the shared bus resonator is driven with a coherent tone. The qubit's transition frequency splits into distinct peaks, with each peak corresponding to a Fock state $|n\rangle$ of the resonator. This measurement confirms the dispersive coupling between the qubit and resonator and allows for extraction of the dispersive shift χ , which is then used to calculate the coupling strength h_j .

THEORY

In this section, we detail the theoretical derivation of the effective Hamiltonian that governs the parametric interaction in our system. We begin by considering a system comprising n fixed-frequency transmon qubits coupled to a frequency-tunable transmon via a shared bus resonator. The full system Hamiltonian in the laboratory frame can be written as:

$$\begin{aligned} H = & \sum_{j=1}^n (\omega_j a_j^\dagger a_j + \frac{\alpha_j}{2} a_j^\dagger a_j^\dagger a_j a_j) + (\omega_0 a_0^\dagger a_0 + \frac{\alpha_0}{2} a_0^\dagger a_0^\dagger a_0 a_0) \\ & + \sum_{j=1}^n g_j (a_0 a_j^\dagger + a_j a_0^\dagger) \\ = & H_q + H_a + H_c \end{aligned} \quad (\text{S1})$$

where a_j^\dagger and a_j are the creation and annihilation operators for the j -th qubit, ω_j is its angular frequency, and α_j is its anharmonicity. The subscript $j = 0$ denotes the frequency tunable qubit (common qubit). The final term describes the exchange-type interaction between the tunable qubit and the other qubits. This effective coupling strength, g_j , arises from a virtual photon exchange mediated by the bus resonator. In the dispersive regime, where the qubit-resonator detunings are large compared to their coupling strengths, a second-order Schrieffer-Wolff transformation yields $g_j \approx \frac{h_0 h_j}{2} \left(\frac{1}{\omega_0 - \omega_b} + \frac{1}{\omega_j - \omega_b} \right)$, where h_j is the coupling strength between the qubit Q_j and the bus resonator, and ω_b is the frequency of the bus resonator.

To simplify the analysis by removing the fast-oscillating free-evolution terms, we transition to an interaction picture defined by the free Hamiltonian of the qubits, $H_{\text{free}} = \sum_{j=0}^n \omega_j a_j^\dagger a_j$. The transformation is given by $U_1 = \exp(-itH_{\text{free}})$, which yields the Hamiltonian:

$$H = \sum_{j=0}^n \frac{\alpha_j}{2} a_j^\dagger a_j^\dagger a_j a_j + \sum_{j=1}^n g_j (a_0 a_j^\dagger e^{i\Delta_j t} + a_j a_0^\dagger e^{-i\Delta_j t}) \quad (\text{S2})$$

where $\Delta_j = \omega_j - \omega_0$ is the detuning between the j -th qubit and the tunable qubit. Our parametric modulation is realized by applying an oscillating flux bias to the tunable qubit, which modulates its transition frequency, $\omega_0(t)$. This introduces a time-dependent driving term to the Hamiltonian. Because this term is diagonal in the qubit basis (proportional to $a_0^\dagger a_0$), it commutes with the transformation U_1 and can be added directly to the Hamiltonian in Equation (S2). Assuming a separate drive tone for each targeted interaction, the Hamiltonian becomes:

$$\begin{aligned} H = & \sum_{j=0}^n \frac{\alpha_j}{2} a_j^\dagger a_j^\dagger a_j a_j + \sum_{j=1}^n g_j (a_0 a_j^\dagger e^{i\Delta_j t} + a_j a_0^\dagger e^{-i\Delta_j t}) \\ & + \sum_{j=1}^n \Omega_j \sin(\nu_j t + \phi_j) a_0^\dagger a_0 \end{aligned} \quad (\text{S3})$$

with Ω_j and ν_j being the amplitude and frequency of the flux modulation, respectively. To absorb the driving term into the coupling part of the Hamiltonian, we move into a second interaction picture defined by the transformation $U_2 = \exp(-i \int H_{\text{drive}}(t') dt')$:

$$\begin{aligned} U_2 = & \text{Exp} \left(-i \int \sum_{j=1}^n \Omega_j \sin(\nu_j t + \phi_j) a_0^\dagger a_0 dt \right) \\ = & \text{Exp} \left(i \sum_{j=1}^n \epsilon_j \cos(\nu_j t + \phi_j) a_0^\dagger a_0 \right) \end{aligned} \quad (\text{S4})$$

with $\epsilon_j = \Omega_j / \nu_j$ being the dimensionless modulation amplitude. After applying this transformation and truncating the Hilbert space to the qubit manifold (thereby ignoring effects related to higher energy levels and the anharmonicity

terms α_j), the Hamiltonian becomes:

$$H = \sum_{j=1}^n g_j (a_0 a_j^\dagger e^{i\Delta_j t} e^{i\xi} + a_j a_0^\dagger e^{-i\Delta_j t} e^{-i\xi}) \quad (\text{S5})$$

where for simplicity we define $\xi = \sum_{j=1}^n \epsilon_j \cos(\nu_j t + \phi_j)$.

The time dependence in the exponents can be eliminated by choosing the modulation frequency for each interaction to be resonant with the qubit detuning, i.e., $\nu_j = \Delta_j$. We now apply the Jacobi-Anger expansion to the exponential terms: $e^{i\epsilon \cos(\theta)} = \sum_{k=-\infty}^{\infty} i^k J_k(\epsilon) e^{ik\theta}$. Substituting this into Equation (S5) produces terms that oscillate at various harmonics of the drive frequencies. By invoking the rotating-wave approximation (RWA), we neglect all rapidly oscillating terms and retain only the time-independent (resonant) components. This yields the final effective Hamiltonian:

$$H = \sum_{j=1}^n g_j J_1(\epsilon_j) \prod_{k \neq j} J_0(\epsilon_k) (i a_0 a_j^\dagger e^{i\phi_j} + h.c.) \quad (\text{S6})$$

This coupling Hamiltonian in Equation S6 can realize an iSWAP-like entangling gate between the tunable qubit and each of the other qubits when choosing proper modulation amplitude and time duration.

This effective Hamiltonian describes a controllable exchange interaction with an effective coupling strength $g_{j,\text{eff}} = g_j J_1(\epsilon_j) \prod_{k \neq j} J_0(\epsilon_k)$, where J_n are Bessel functions of the first kind. The product term reflects the AC Stark shift induced by the other simultaneous drive tones. By tuning the modulation amplitudes ϵ_j and the interaction time t , we can engineer a desired unitary evolution. Specifically, for a two-qubit interaction, setting the initial phase of the drive to $\phi_j = -\pi/2$ transforms the Hamiltonian into the form $H_{\text{eff}} = g_{j,\text{eff}} (a_0 a_j^\dagger + a_j a_0^\dagger)$. An evolution under this Hamiltonian for a time $t = \pi/(4g_{j,\text{eff}})$ ideally generates the $\sqrt{\text{iSWAP}}$ gate, which is the subject of our experimental investigation.

In practice, the phase of this gate requires careful tuning. The additional phase accumulated by the qubits from their free evolution, which is tracked in the rotating frame defined by the transformation U_1 , can be compensated by applying single-qubit virtual z -rotations. However, applying such rotations is mathematically equivalent to shifting the temporal origin of the entire gate sequence. Therefore, the essential tuning parameter for the interaction basis itself is the initial phase, ϕ_j , of the parametric pulse. We optimize this parameter directly and, for the first gate in a sequence, set it to $\phi_j = -\pi/2$ to realize the desired $\sqrt{\text{iSWAP}}$ operation. For subsequent gates in a sequence, this phase must be advanced accordingly to account for the evolution that occurred during the preceding gates.

CALIBRATION OF PARAMETRIC DRIVE AMPLITUDE AND FREQUENCY

In our experiment, we measure the simultaneous quantum-state population of all qubits as a function of gate length and drive frequency by applying a parametric modulation pulse on the common qubit. This parametric flux modulation induces a DC shift in the common qubit's frequency, thereby shifting the resonant exchange frequency from its un-driven value, $\nu_{j,\Omega_j=0}$. Relative to the detuning between each computational qubit and the common qubit, we observe drive frequency offsets of 8.3 MHz, 7.6 MHz, and 10.8 MHz for the two-, three-, and four-qubit cases, respectively. These offsets vary with the amplitude of the parametric drive. At the offset driving frequency, coherent exchange between qubits exhibits slower oscillation but higher inter-qubit exchange. Deviating from this frequency results in faster oscillation and degraded quantum exchange, as shown in the Chevron pattern (Figure 2(e)) as an example.

We tune both the parametric drive amplitude and frequency to find a condition, which yields a maximum inter-qubit exchange with the slowest exchange oscillation. Accordingly, we define the “oscillation period” as the period of exchange oscillation (a full population swap) along the cut line corresponding to the offset drive frequency. This period changes with drive amplitude. In practice, we select a drive amplitude with corresponding frequency that give the shortest oscillation period as a reference driving power. Figure S4 shows the variation of oscillation period with driving power relative to the reference. The data indicate that the oscillation period initially decreases with increasing drive power, reaches a minimum, and then increases again.

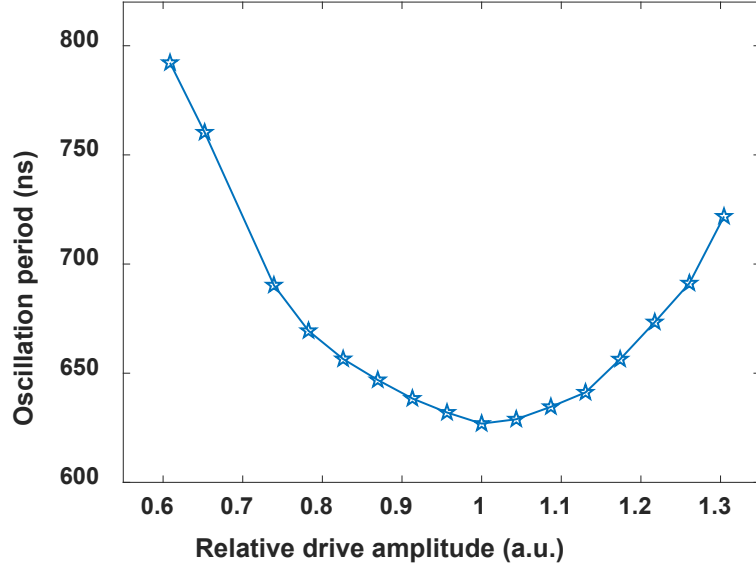


FIG. S4. **Calibration of the parametric drive amplitude.** The oscillation period of a full population swap between Q_0 and Q_1 is plotted as a function of the relative amplitude of the parametric drive. The period is inversely proportional to the effective coupling strength g_{eff} . The optimal drive amplitude is chosen at the minimum of the oscillation period, which corresponds to the maximum coupling strength and fastest gate speed.

XEB

To evaluate the state preparation and measurement (SPAM) error-free fidelity of the \sqrt{iSWAP} gate, which is not an element of the Clifford group, we perform cross-entropy benchmarking (XEB). The XEB protocol involves applying sequences of random single-qubit rotations chosen from a set of 64 distinct single-qubit gates. Each gate is a combination of a $\frac{\pi}{2}$ rotation around an axis in the xy-plane at $\frac{n\pi}{8}$ and a Z-rotation of $\frac{n\pi}{8}$, where $n = 0, 1, \dots, 7$. By measuring the output bitstrings $\{x_i\}$ for each gate sequence, we calculate the standard XEB fidelity, F_{XEB} , as defined in Equation S7, where $p(x_i)$ is the probability of observing the bitstring x_i .

$$F_{XEB} = \frac{H(p_{uni}, p_{th}) - H(p_{exp}, p_{th})}{H(p_{uni}, p_{th}) - H(p_{th}, p_{th})} \quad (S7a)$$

$$H(p, q) = - \sum_{\{x_i\}} p(x_i) \log_2 q(x_i) \quad (S7b)$$

During the XEB experiment, we observe that the gate fidelity is highly sensitive to phase errors in the parametric pulse. This pulse is synthesized based on the pre-calibrated qubit spectrum, an approach that implicitly assumes an ideal, instantaneous response from the flux control line. However, non-negligible distortion and delay within the control system introduce additional errors to the \sqrt{iSWAP} gate. As these errors accumulate throughout the duration of the two-qubit gate, they cannot be compensated by subsequent single-qubit operations. Therefore, a precise calibration of the qubit's z-control line response is crucial.

To this end, we employ a Cryoscope protocol to characterize the actual flux, Φ_Q , at the chip level[42]. The Cryoscope is a Ramsey-like experiment wherein square flux pulses of varying lengths, but constant amplitude, are embedded between two $\frac{\pi}{2}$ pulses. By measuring the accumulated qubit phase, ϕ , induced by the off-idle pulse, we can determine the on-chip frequency detuning via the relation $\frac{\Delta\phi}{\Delta t}$. This frequency detuning is then converted to a flux value using the pre-calibrated qubit spectrum, yielding response data with a temporal resolution set by the time domain resolution of the flux pulse.

Informed by the frequency response data, we design a set of digital pre-distortion filters to compensate for the phase errors. For long-timescale distortions (>10 ns), such as overshoot, undershoot, and slow drift of the flux pulse, we implement infinite impulse response (IIR) filters. For short-timescale effects (<10 ns), including fast oscillations arising from the limited bandwidth of the control system and residual errors from the IIR filters, we utilize finite

impulse response (FIR) filters. The efficiency of these filters is verified by routing the pre-distorted flux pulses back into the Cryoscope experiment. Both IIR and FIR filters tend to temporally extend the pulse on the order of the overshoot/undershoot; we mitigate this effect by introducing additional idle time before and after the flux pulse.

Three degrees of freedom are available for phase tuning during the XEB experiment: virtual z -rotations applied to each qubit following the $\sqrt{i\text{SWAP}}$ gate, and the initial phase of the parametric pulse. The first two are straightforward, as our parametric pulse ideally generates a $\sqrt{i\text{SWAP}}$ gate up to single-qubit rotations. The third degree of freedom corresponds to the initial phase of the parametric drive in the Hamiltonian. Several considerations are pertinent to this phase calibration. First, the phase of our parametric pulse must compensate for the phase accumulated due to the detuning of the two qubits from their physical interaction idle frequency point. The frequency of the applied pulse, however, is slightly different from the qubit detuning. The dynamical part of the initial phase depends solely on the qubit detuning, not the applied frequency. Second, the initial phase is related to the pulse's temporal ordering, since virtual z -rotations after the gate are equivalent to choosing a distinct temporal starting point. Consequently, we must adjust the initial phase of each parametric pulse in addition to the dynamical one. Through the comprehensive calibration and optimization procedures described above, we achieve an average XEB fidelity of 94.54(38)% for the $\sqrt{i\text{SWAP}}$ gate. We attribute the primary source of infidelity to the decoherence error.

CRYOSCOPE MEASUREMENT

The fidelity of parametrically activated gates is critically dependent on the precise, time-domain control of the qubit frequency. Non-ideal components in the control electronics, such as amplifiers and cables, inevitably introduce distortions to the flux pulses, leading to coherent control errors. To mitigate these effects, we first characterize the on-chip pulse shape using a Cryoscope protocol and then apply digital pre-distortion filters to the input waveform [42].

As described in the main text, the Cryoscope protocol is a Ramsey-like experiment designed to measure the time-resolved frequency shift induced by a flux pulse. The sequence consists of two $\frac{\pi}{2}$ pulses separated by a fixed time interval, with a square flux pulse of variable duration, τ , embedded within this interval. By sweeping the pulse duration τ and measuring the expectation values $\langle \sigma_x \rangle$ and $\langle \sigma_y \rangle$ of the qubit after the final $\frac{\pi}{2}$ pulse, we reconstruct the total accumulated phase, $\phi(\tau)$.

The raw phase data contains both the desired signal from the pulse-induced detuning and high-frequency oscillations. To isolate the former, we perform a series of post-processing steps. First, a Fourier transform is applied to the phase data, $\phi(\tau)$, to identify the dominant oscillation frequency, which corresponds to the static detuning of the qubit from its idle point. This frequency is used to demodulate the signal, effectively removing the large-scale Ramsey fringes and highlighting the subtle deviations caused by pulse distortions. Subsequently, a second-order Savitzky-Golay filter is applied to the demodulated phase data. This smooths the signal while preserving its features and allows for a robust numerical calculation of the derivative, $\frac{d\phi}{d\tau}$, which is directly proportional to the instantaneous frequency detuning. Finally, using a pre-calibrated qubit flux-frequency map, we convert this time-resolved frequency detuning into the effective on-chip flux pulse shape, $\Phi_Q(\tau)$.

With the measured pulse response, we design digital filters to pre-distort the input waveform such that the on-chip pulse becomes as close to the ideal square pulse as possible. We employ a combination of infinite impulse response (IIR) and finite impulse response (FIR) filters, which can both be described by the general linear difference equation:

$$a_0 y[n] = \sum_{i=0}^N b_i x[n-i] - \sum_{j=1}^M a_j y[n-j] \quad (\text{S8})$$

where $x[n]$ is the discrete input signal and $y[n]$ is the discrete output signal (pre-distorted pulse). FIR filters are non-recursive ($a_j = 0$ for $j \geq 1$), whereas IIR filters are recursive.

We use IIR filters to compensate for long-timescale distortions (>10 ns), such as exponential undershoots, which can be modeled as a single-pole decay. For a step function response $\eta(t)$ distorted by an exponential undershoot of the form $s(t) = \eta(t)(1 + Ae^{-t/\tau_{\text{IIR}}})$, the corresponding coefficients for a discrete-time IIR filter that inverts this response can be analytically derived:

$$a_0 = 1 \quad (\text{S9a})$$

$$a_1 = \alpha - 1 \quad (\text{S9b})$$

$$b_0 = k\alpha - k + 1 \quad (\text{S9c})$$

$$b_1 = -(\alpha - 1)(k - 1) \quad (\text{S9d})$$

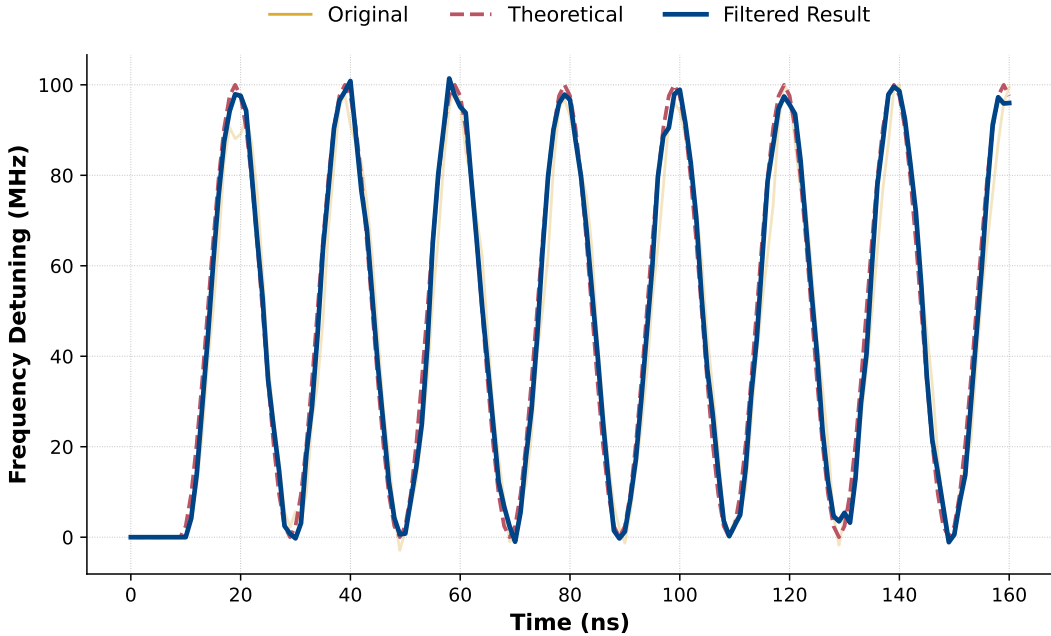


FIG. S5. Verification of pulse shaping for sinusoidal modulation. Cryoscope measurement of the on-chip response to a sinusoidal flux drive. The target waveform, a 50 MHz sinusoid, is shown as a dashed red line. The measured response to this input pulse after correction by the IIR/FIR pre-distortion filters is shown in blue. The excellent agreement demonstrates the filter's efficacy in producing high-fidelity, time-varying frequency modulation at the chip level.

where $\alpha = 1 - \exp(1/(f_s \tau_{\text{IIR}}(A + 1)))$, $k = -1/((A + 1)(\alpha - 1))$ for an undershoot ($A < 0$), and f_s is the sampling rate of our arbitrary waveform generator.

We use FIR filters to correct for short-time scale (< 10 ns) distortions, such as fast oscillations (ringing) from limited bandwidth and any residual errors introduced by the IIR filter. Lacking a simple analytical model for these distortions, we numerically optimize the FIR filter coefficients $\{b_i\}$. We employ the Covariance Matrix Adaptation Evolution Strategy (CMA-ES) algorithm to find the 7 filter taps that minimize the mean squared error between the ideal square pulse and the experimentally measured on-chip response after filtering.

The efficiency of these filters is verified by routing the pre-distorted flux pulses back into the Cryoscope experiment. We choose the same DC flux bias as in the two-qubit gate experiment, applying parametric pulses with an amplitude corresponding to a 50 MHz frequency shift ($f_{pp} = 100$ MHz) and 50 MHz in time domain. The Cryoscope results before and after the pre-distortion are shown in [Figure S5](#).

QST DATA FOR Q_0 - Q_2

[Figure S6](#) (a) and (b) show a representative two-qubit state density matrix for Q_0 - Q_2 .

DECOHERENCE ERROR

Given the gate duration of 320-720 ns, decoherence represents a primary source of infidelity for the $\sqrt{i\text{SWAP}}$ operation. In this section, we develop a theoretical model to quantify the impact of environmental noise on the gate fidelity. We model this decoherence by considering two independent noise channels acting on the qubits: energy relaxation (amplitude damping) and pure dephasing (phase damping).

The effect of these noise processes is quantified using the Kraus operator formalism. The average fidelity of a noise channel, which describes how well the channel preserves an arbitrary input state on average, is given by [2]:

$$F = \frac{d + \sum_k |\text{Tr}(E_k)|^2}{d(d + 1)} \quad (\text{S10})$$

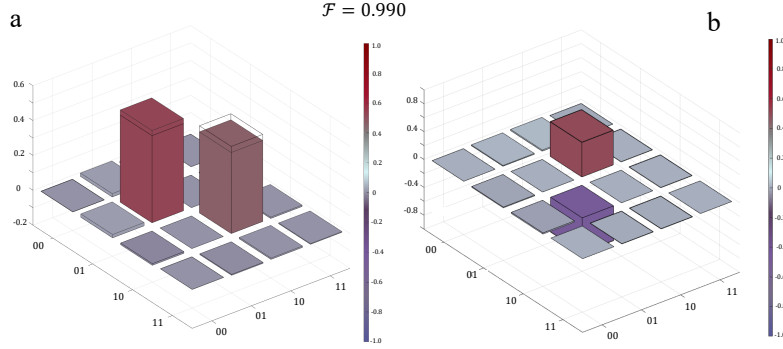


FIG. S6. **QST for Q_0 - Q_2 .** Real part (a) and imaginary part (b) of a reconstructed 2-qubit density matrix for Q_0 - Q_2 ($F = 0.990(2)$, $t_{gate} = 365$ ns). Experimental results (colored bars) are compared to the ideal state (transparent bars).

where d is the dimension of the Hilbert space and $\{E_k\}$ are the Kraus operators that define the noise channel, satisfying the completeness relation $\sum_k E_k^\dagger E_k = I$. Note that we have simplified the trace term using this relation.

For a single qubit, we define the probabilities of a relaxation or dephasing event occurring during the gate time t as:

$$\text{Amplitude Damping Probability: } p_1 = 1 - e^{-t/T_1}$$

$$\text{Phase Damping Probability: } p_\phi = \frac{1}{2}(1 - e^{-t/T_\phi})$$

where T_1 is the energy relaxation time and T_ϕ is the pure dephasing time. For gate times $t \ll T_1, T_\phi$, we can use the first-order approximations $p_1 \approx t/T_1$ and $p_\phi \approx t/(2T_\phi)$. The Kraus operators for these single-qubit channels are:

$$\text{Amplitude Damping: } E_0 = \begin{pmatrix} 1 & 0 \\ 0 & \sqrt{1-p_1} \end{pmatrix}, \quad (\text{S11a})$$

$$E_1 = \begin{pmatrix} 0 & \sqrt{p_1} \\ 0 & 0 \end{pmatrix} \quad (\text{S11b})$$

$$\text{Phase Damping: } E_2 = \begin{pmatrix} \sqrt{1-p_\phi} & 0 \\ 0 & \sqrt{1-p_\phi} \end{pmatrix}, \quad (\text{S11c})$$

$$E_3 = \begin{pmatrix} \sqrt{p_\phi} & 0 \\ 0 & -\sqrt{p_\phi} \end{pmatrix} \quad (\text{S11d})$$

To model the decoherence on an N -qubit system, we assume that the noise acts independently on each qubit. The total noise channel is thus a tensor product of single-qubit channels, where the non-trivial Kraus operators act on one qubit while the identity operator acts on the others. By constructing the multi-qubit Kraus operators for each channel and substituting them into [Equation S10](#), we derive the average fidelity for systems of 2, 3, and 4 qubits. The resulting fidelities, keeping only the first-order terms in t/T_1 and t/T_ϕ , are summarized in [Table S1](#).

TABLE S1. Average state fidelity under amplitude damping and phase damping for different qubit numbers.

Qubit number	2	3	4
Amplitude damping	$1 - \frac{2t}{5T_1}$	$1 - \frac{4t}{9T_1}$	$1 - \frac{8t}{17T_1}$
Phase damping	$1 - \frac{2t}{5T_\phi}$	$1 - \frac{4t}{9T_\phi}$	$1 - \frac{8t}{17T_\phi}$

NUMERICAL SIMULATIONS

Using Qutip in PYTHON [55], we perform numerical simulations with the Hamiltonian in [Equation S13](#), which accounts for higher-level states by truncating each qubit's energy spectrum to three levels. Here, ω_j denotes the frequency of Q_j , $g_{0,j}$ is the coupling strength between Q_j and Q_0 , and $g_{0,j} = \frac{h_0 h_j}{2} \left(\frac{1}{\Delta_{0,b}} + \frac{1}{\Delta_{j,b}} \right)$, where $\Delta_{j,b} = \omega_j - \omega_b$. The parameters ω_j and ν_j represent the amplitude and frequency of the parametric drive applied to the qubit pair Q_0 - Q_j , and α_j is the anharmonicity of Q_j . The fifth and sixth terms correspond, respectively, to random flux noise, denoted $S_\phi^{(random)}$, and the static ZZ interaction ξ_{ZZ}^j between Q_j and Q_0 .

We model the environmental flux noise as a characteristic $1/f$ power spectral density (PSD), given by $S_\phi(f) = A_\Phi/f$ [1]. The noise amplitude, A_Φ , is an experimentally determined parameter extracted from independent Ramsey and echo T2 measurements on the common qubit. From this PSD, we can generate representative time-domain noise traces.

The impact of $1/f$ noise is dominated by its low-frequency components. For a gate of duration t_{gate} , noise components with frequencies $f \ll 1/t_{\text{gate}}$ do not average out and act as a quasi-static frequency offset on the qubit. This offset is effectively constant during a single experimental shot but varies from shot to shot. We therefore model this dominant noise effect by sampling a random frequency offset, $\delta\omega$, from a Gaussian distribution with zero mean and a variance, σ^2 , given by the integrated noise power:

$$\sigma^2 = \int_{f_{\text{low}}}^{1/t_{\text{gate}}} S_\phi(f) df \quad (\text{S12})$$

The integration runs from a low-frequency cutoff of $f_{\text{low}} = 10^{-4}$ Hz up to the frequency corresponding to the gate's timescale (The high cutoff frequency is set to be about 3 GHz. But for $1/f$ noise, the power at high frequencies drops off so quickly that the contribution above 1-2 GHz is negligible).

The random flux noise, $S_\phi^{(random)}$, is generated as a random waveform based on the experimentally extracted flux-noise spectral density of $S_\phi = (2.45\mu\phi_0)^2/\text{Hz}$. Our simulations account for qubit decoherence, dephasing, flux noise, and static ZZ interactions, with all simulation parameters set to their experimentally measured values.

$$\begin{aligned} H = & \sum_{j=0}^n \omega_j a_j^\dagger a_j + \sum_{j=0}^n \frac{\alpha_j}{2} a_j^\dagger a_j^\dagger a_j a_j + \sum_{j=1}^n g_j (a_0 a_j^\dagger e^{i\Delta_j t + h.c.}) \\ & + \sum_{j=1}^n \Omega_j \sin(\nu_j t + \phi_j) a_0^\dagger a_0 + S_\phi^{(random)}(t) a_0^\dagger a_0 + \sum_{j=1}^n \xi_{ZZ}^j a_0^\dagger a_0^\dagger a_0 a_0 \end{aligned} \quad (\text{S13})$$

The error infidelities arising from flux noise and ZZ interactions are extracted by comparing the fidelity with and without the corresponding noise channel. We first simulate the time evolution of the Hamiltonian under experimental conditions for systems of two, three, and four qubits. The simulated qubit occupation probabilities during multi-qubit exchange oscillations are shown in [Figure 3\(a\)](#). These simulation results are consistent with the experimental data.

We next perform quantum state tomography (QST) and gate simulations to extract the error infidelity contributed by each individual noise channel, summarizing the results in Table I in the main text. The state fidelity is calculated with $F(\rho, \sigma) = \sqrt{\sqrt{\rho}\sigma\sqrt{\rho}}$, where σ is the density matrix of the ideal final state and ρ is the simulated density matrix. The gate fidelity is then estimated by averaging the state fidelities over the 36 two qubit initial states that are formed from the tensor product of the six standard single qubit states, $\{|0\rangle, |1\rangle, \frac{1}{\sqrt{2}}(|0\rangle \pm |1\rangle), \frac{1}{\sqrt{2}}(|0\rangle \pm i|1\rangle)\}^{\otimes 2}$. We also simulate the evolution of the gate unitary operator and extract the gate fidelity at the gate time when the entanglement reaches its maximum. The simulation is performed by modeling each transmon as a three-level system (qutrit) to account for potential leakage to the non-computational $|2\rangle$ state. We then perform a Monte Carlo estimation of the noise-induced infidelity. For each run, a static frequency offset, sampled from the Gaussian distribution described above, is added to the common qubit's Hamiltonian, and the full unitary evolution is simulated. By averaging the process fidelity over 1000 such noise realizations, we determine the average infidelity contribution from low-frequency flux noise.

The results of this analysis, combined with the other simulated error channels, are summarized in Table I in the main text. This comprehensive breakdown shows that the infidelity from flux noise, ϵ_{flux} , is on the order of 10^{-3} to 10^{-4} , confirming that it is a sub-dominant error source compared to qubit decoherence and coherent control errors for our current device.

To verify the potential of our parametric global gate scheme, we simulate the generation of entangled states in systems of two to six qubits using state of the art superconducting qubit parameters. The six qubits Q_0 - Q_5 have frequencies $\omega_j/2\pi = 5.0, 5.25, 5.18, 5.10, 5.06$, and 5.03 GHz for $j = 0 \sim 5$, respectively, and the resonator frequency is $\omega_b/2\pi=5.40$ GHz, with Q_0 serving as the common qubit. We take into account qubit decoherence, dephasing, flux noise, and static ZZ interactions for the simulation. We assign a relaxation time and a dephasing time of $60 \mu\text{s}$ to all qubits, representing an achievable decoherence benchmark for current processors, and apply a static ZZ coupling $\frac{\xi_{ZZ}}{2\pi} = 2.5 \times 10^4$ Hz between the common qubit and each computational qubit ($j = 1 \sim 5$). The flux noise spectral density is set to $S_\phi = (2.45\mu\phi_0)^2/\text{Hz}$, consistent with the values used in real device simulations.

The resulting multi qubit exchange oscillations for systems of two to six qubits are shown in [Figure S7](#). At the points of maximum entanglement (indicated by black arrows), we obtain high state fidelities of 99.91%, 99.88%, 99.85%, 99.80%, and 99.70%, respectively.

TABLE S2. Device parameters

	Q_0	Q_1	Q_2	Q_3	Bus resonator
$\omega_r/2\pi(\text{GHz})$	7.00075	7.0229	7.03875	7.0777	5.5208
$\omega_j/2\pi(\text{GHz})$	5.0408 ^a 5.1941 ^b	5.0992	5.2056	5.2347 ^a 5.3928 ^b	—
$g_{r,j}/2\pi(\text{MHz})$	83.9	86.2	90.0	54.4	—
$T_1(\mu\text{s})$	30.4 ^a	31.7	38.5	33.2 ^a	—
$T_2^{Ramsey}(\mu\text{s})$	5.1 ^a	25.3	31.0	2.6 ^a	—
$T_2^{Echo}(\mu\text{s})$	17.3 ^a	44.1	40.3	16.6 ^a	—
$g_j/2\pi(\text{MHz})$	17.3	22.8	18.2	15.2	—
$\xi_{ZZ}/2\pi(\text{kHz})$	—	26.2	30.1	28.0	—
$\alpha_j(\text{MHz})$	-209.8	-209.3	-210.2	-204.3	—

^a off sweetspot

^b on sweetspot

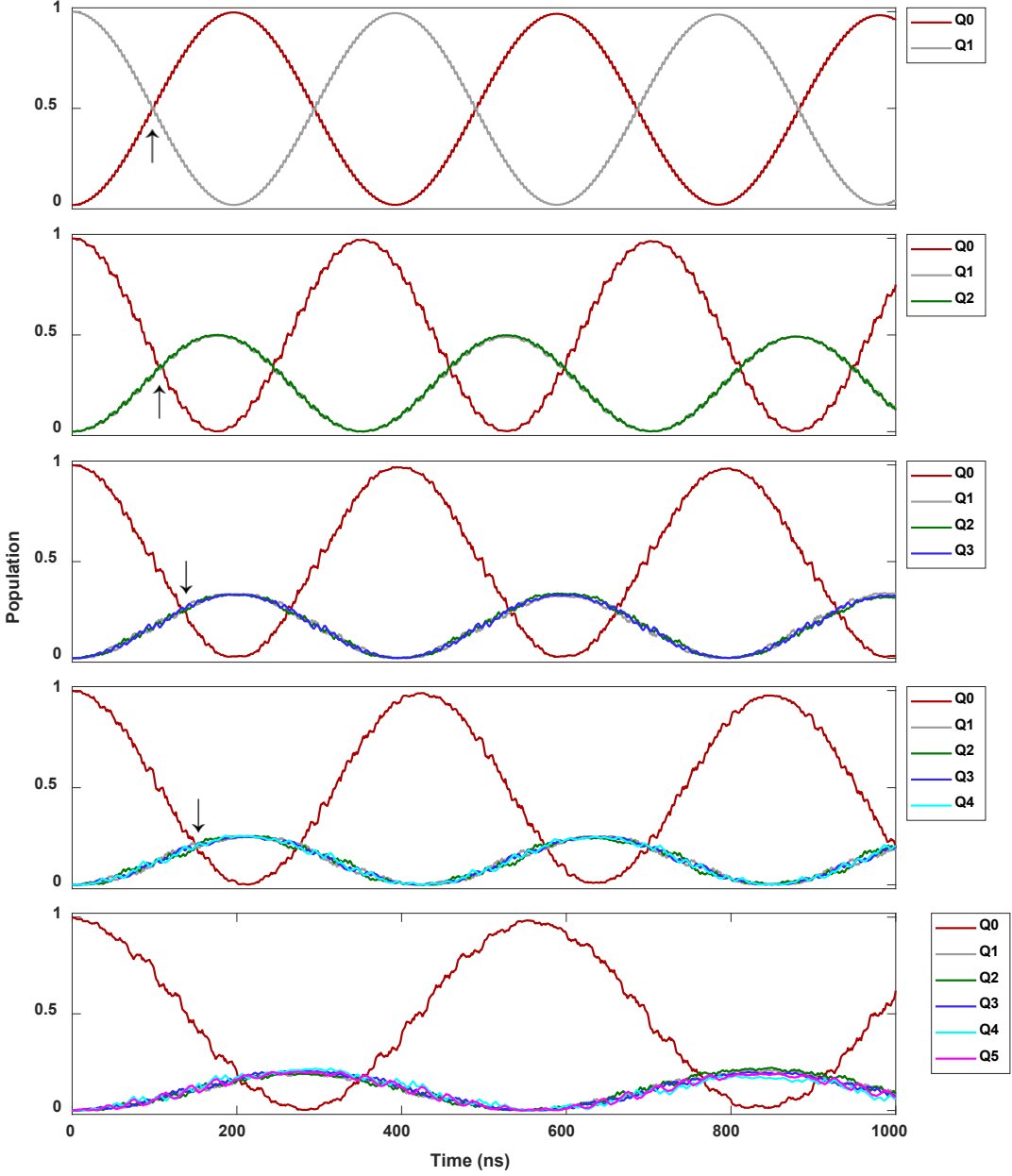


FIG. S7. Simulated generation of multi-qubit W-states. The population dynamics of systems from two to six qubits are shown under a global parametric drive. The system is initialized in the state $|10\cdots0\rangle$. The drive induces coherent oscillations that distribute the single excitation among all participating qubits. The black arrows indicate the time when the system first reaches a state of maximum entanglement (an equal-superposition W-state), at which the state fidelities are extracted. Simulation parameters: Bus resonator frequency: $\omega_b/2\pi=5.40$ GHz; Qubit frequency: $\omega_j/2\pi = 5.0, 5.25, 5.18, 5.10, 5.06, 5.03$ GHz, $h_j/2\pi=28$ MHz, $\alpha_j = -200$ MHz, $\frac{\xi_{zz}}{2\pi} = 2.5 \times 10^4$ Hz for $j = 0 \sim 5$; $T_1 = 60 \mu\text{s}$ and $T_2\text{Echo} = 60 \mu\text{s}$; $S_\phi = 2.45\mu\phi_0/\sqrt{\text{Hz}}$ Two-qubit case: $\Omega_1/2\pi=1200$ MHz; Three -qubit case: $\Omega_1/2\pi=1200$ MHz, $\Omega_1:\Omega_2=1:0.9$; Four-qubit case: $\Omega_1/2\pi=980$ MHz, $\Omega_1:\Omega_2:\Omega_3=1:0.91:0.59$; Five-qubit case: $\Omega_1/2\pi=820$ MHz, $\Omega_1:\Omega_2:\Omega_3:\Omega_4=1:0.89:0.6:0.36$; Six-qubit case: $\Omega_1/2\pi=1000$ MHz, $\Omega_1:\Omega_2:\Omega_3:\Omega_4:\Omega_5=1:0.76:0.49:0.19:0.2$.